Chapter 4

Raman effect and unusual transport properties of narrow band gap semiconductor Heusler alloy

4.1 Introduction

Thermoelectric materials have the potential to play a crucial role in addressing today's energy and environmental challenges (Champier (2017)). With the increasing demand for energy, the efficient conversion of waste heat into electrical energy has become a priority. Thermoelectric materials can convert waste heat from various sources, including industrial processes and vehicle engines, into usable electricity. This reduces energy waste, increases efficiency, and offers a practical solution to reduce carbon emissions. As the research in thermoelectric materials advances, the potential for energy-efficient and environmentally friendly technologies will continue to increase, providing a promising future for clean energy solutions. From the application perspective, a large thermopower at room temperature is required, for which heavily doped semiconductors are the favorable choice. The well-known system for providing high thermopower is topological insulator

Bi_2Te_3 (Matsushita et al. (2017)). However, the hazardous nature of Te limits its use for application purposes. Considering this, Heusler alloys emerge as a good alternative (Hinterleitner et al. (2020); Jiang & Yang (2021); Lue et al. (2007); Mondal et al. (2018); Nakatsugawa et al. (2020)).

In Heusler alloys, the thermopower can be tuned by utilizing the substitution method. These alloys with the general formula X_2YZ consist of transition metal elements (X,Y) and *p*-block elements (Z). Therefore, if the substitution is made at *Z*- site, then due to the doping of *n*-type and *p*-type material, the Fermi level shifts up or down respectively. This does not change the electronic structure, but the position of the Fermi level is important for enhancing the value of the Seebeck coefficient (S) (Hayashi et al. (2020)). Similarly, if the partial substitution is made at the *X* site, it will change the electronic structure of the system (Garmroudi et al. (2022)), aiding in the improvement of thermoelectric properties. Consequently, Heusler alloys serve as an excellent replacement for devices based on thermoelectric materials.

The *Mn*-based Heusler alloys exhibit a positive *S* (Bhat et al. (2015); Seredina et al. (2019); Yousuf & Gupta (2018)). For instance, Mn_2VAl demonstrates a positive *S* from 315 K to 717 K (Li et al. (2020)), while Mn_2CoSn displays positive *S* only up to 137 K before transitioning to an *n*-type behavior. The revolutionary spin gapless system, Mn_2CoAl, (Ouardi et al. (2013)) also demonstrates a positive *S* over a specific temperature range. *Mn*-based Heusler alloys have shown a consistent trend towards a positive *S*, albeit with varying temperature ranges and unique characteristics like switching from n to *p*-type, an almost constant value of *S*.

This work focuses on studying the thermopower of *Co*-doped Mn_2FeAl. The efficiency of a thermoelectric is expressed from its figure of merit, $ZT = \frac{S^2T}{\rho\kappa}$, where, ρ and κ are the electrical resistivities and thermal conductivity of the system, respectively. To enhance the efficiency of a system, the electrical conductivity (σ) needs to increase, and κ

needs to decrease simultaneously. For the system, σ is increased compared to the parent system (Gavrikov et al. (2019)) due to Co doping and the value of K is decreased at room temperature in comparison to the Mn_2VAl system (Li et al. (2018)). The temperature-dependent Raman spectrum of the system is also measured. In order to confirm the doping and purity of the system, the X-ray photoemission spectrum (XPS) of the alloy is also recorded.

4.2 Experimental Details

The polycrystalline MCFA sample is prepared by the standard arc melting process as described in the previous paper (Dixit et al. (2023)). The temperature-dependent Raman spectrum was measured by a Horiba LabRam HR evolution spectrometer. An excitation wavelength of 633 nm was used from a $He-Ne$ laser manufactured by Horiba Instrument Inc. For thermoelectric measurement, a handmade setup was used. In which the sample is sandwiched between the two copper plates, and one plate is connected to the heater while the other one is in contact with the cryostat, which makes it cool. For the X-ray photoemission spectroscopy (XPS) technique, the $Al-K\alpha$ X-ray source and the analytical aperture of diameter $400\mu m$ were used. For transport properties, a rectangular-shaped sample is used. The resistivity is measured using four probe method, and probes are made by using the silver paste. It consists of a He-cooled closed cycle refrigerator (CCR), Lake Shore (model- 325) temperature controller and Keithly 2400 SoureMeter is used in a 4-wire sense configuration to measure the resistance of the system.

4.3 Results and Discussions

4.3.1 X-ray photoemission spectroscopy (XPS) study

XPS is performed of $Mn_{1.5}Co_{0.5}FeAl$ (MCFA) alloy to determine the electronic state of elements. The survey scan of the MCFA is shown in figure 4.1 indicates the presence of all elements. Based on the National Institute of Standards and Technology (NIST) XPS database, all the peaks and doublet separations have been determined (Briggs (2006); Naumkin et al. (2012)). According to the survey scan *Mn*, *Fe*, *Co*, and *Al* are present in the sample. Using the XPSPEAKFIT software, peaks of all elements are deconvoluted to examine the existence of various metallic states. Figure4.1 (a) displays the XPS spectrum of *Mn* along with the deconvoluted spectrum. It contains two main peaks positioned at 641.8 eV and 653.3 eV binding energies. In deconvoluted spectra, the main peaks have shown mixed states. The peak corresponds to the Mn $2p_{3/2}$ (641.8 eV) having split states with Δ_{ex} = 1.6 eV. The splitting found in the system is directly related to the local magnetic moment at the *Mn* site, which is comparable with the value observed for *Mn* 2p spectra (Plogmann et al. (1999)). Similarly, the peak positioned at 653 eV is deconvoluted into two peaks at 653.3 eV and 654.6 eV validating the presence of local moment at the *Mn* site. The spin-orbit splitting, which is identified as the change in energy between the two main peaks of Mn ($\Delta_{ex} \sim 11.5eV$), arises from the exchange interaction between the core hole and the 3d valance electrons of the *Mn* atom. Other than these two main peaks, the satellite peaks are observed at 5 eV towards higher binding energies from the main peak of the *Mn* states. The observation of satellites implies the presence of *d* character in the unoccupied bands as well as indicates the presence of confined moments at Mn sites (Rednic et al. (2009)). In Mn-based Heusler alloys, the spectra display splitting, suggesting the presence of local moments associated with *Mn*. Transition metal elements typically exhibit delocalized moments; however, when they are in alloy form, they tend to show localization of the moment.

In addition, the XPS spectrum for Co is shown in figure 4.1 (b), here, we observed only one main peak corresponding to the $2p_{3/2}$ (783.6 eV) state, and the satellite peak is observed at a higher binding energy of 5eV. The presence of satellite peak suggests the presence of local moment at Co- sites. Further, the core level XPS spectrum of Fe, shown in figure 4.1 (c), with a deconvoluted spectrum. The spectrum of Fe consists of two main peaks located at 707 eV and 720.2 eV. After deconvolution, the peaks located at 706.9 and 720.2 eV correspond to the $2p_{3/2}$ and $2p_{1/2}$ state of Fe, respectively. While the peak located at 709.9 eV and 722.2 eV corresponds to the $2p_{3/2}$ and $2p_{1/2}$ states of Fe_2O_3 and $Fe(CO)_5$, respectively(Saravanan et al. (2022)). Figure 4.1(d) shows the deconvoluted spectra of Al. For Al, the main peak is located at 73.9 eV, and a shoulder peak is observed at 72.5 eV. The valance band spectrum of the system in figure 4.1(f) shows a broad peak around 4 eV and a shoulder peak at 10 eV. Another main peak in valence spectra is observed at higher binding energies of 14 eV. The broad peak observed at low energy is mainly due to the transition metal elements present in the system, while the second main peak is due to the sp block elements(Plogmann et al. (1999)).

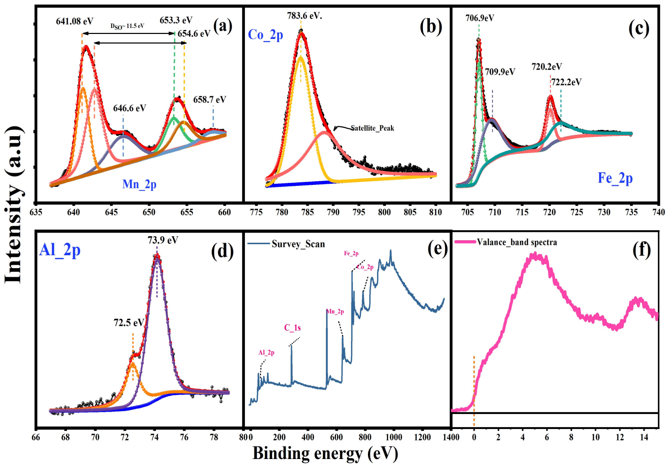

Fig. 4.1 (a-d) X-ray photoemission spectra of Mn, Co, Fe, and Al. (e,f) Survey scan and valance band spectra of $Mn_{1.5}Co_{0.5}FeAl$ alloy.

4.3.2 Analysis of Raman spectroscopy

The Raman spectrum of MCFA is recorded with a source wavelength of 633 nm over the energy range of 350 cm^{-1} to 700 cm^{-1} shown in figure 4.2. At Room temperature Raman spectrum, two peaks were observed; peak B is at 432 cm^{-1} while the other main peak A is at 614 cm^{-1}, indicated by an arrow. Both peaks are fitted with the Lorentzian function by setting width, intensity, and peak position as free parameters. The deconvoluted spectrum, along with the net spectrum (red dotted line) is shown in figure 4.2 (b). Further, the temperature-dependent study of Raman spectra is performed. Here, a change in peak position at 150 K is noticed, attributed to the activation behavior of the charge carriers. Although there are very few experimentally reported Raman spectra for Heusler alloys to date (Zhai et al. (2014); Zhan et al. (2012)). Bera et al. (2022), have observed the Raman peak at 645 cm^{-1} for $NiFeMnSn$ system. In that study, this peak appeared due to crystal field excitations, providing valuable insights into the vibrational properties of Heusler alloys. Typically, Raman peaks in the insulating magnetic system, and for oxide systems (Sharma et al. (2019)) results from either the phonons or magnons. However in metallic systems the density of electrons cloud in the conduction band is high (Rosalin et al. (2023); Wang et al. (2022)). Therefore, Raman spectra showed spectral features due to the electronic excitations (Schaack (2007)). However, most of the Heusler alloys display either half-metallic or metallic properties. Therefore, very few phonons-mediated Raman spectra for Heusler Alloys are reported. The present system exhibited the metallic property. Therefore, the phonon-mediated Raman scattered modes could be absent in MCFA. Furthermore, the peak centre and FWHM with temperature is plotted as given in figure 4.2 (c), (d) respectively. In phonon-mediated spectra, changes in lattice vibrations can alter the peak width with temperature, but as shown in figure 4.2 (d), the peak width remained constant with the temperature. All these findings suggested that the observed Raman spectra could be due to the electronic excitations.

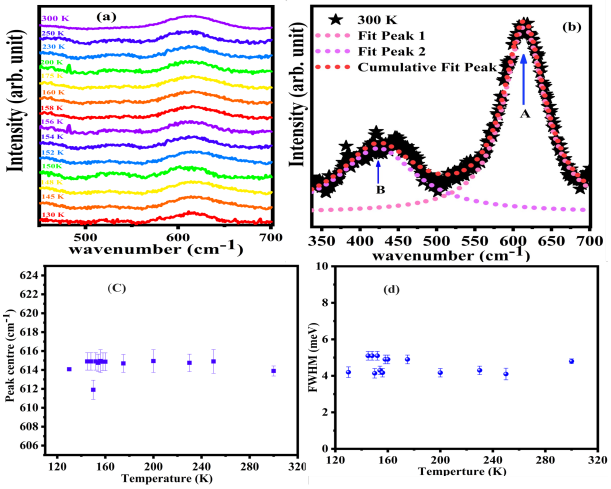

Fig. 4.2 (a) Temperature dependent Raman spectra of $Mn_{1.5}Co_{0.5}FeAl$ using excitation wavelength of 633 nm. (b) Room temperature Raman spectra with Lorentzian fit.t. (c) variation in peak centre position with temperature (d) peak width with temperature

4.3.3 Electrical Resistivity and Weighted Mobility

To understand the mechanism of charge conduction in the system, the temperature-dependent resistivity $\rho(T)$ is measured, shown in figure 4.3 (a). It displays the negative temperature coefficient of resistivity (TCR). The presence of negative TCR in such materials is an indication of the narrow gap of the order of 10 meV (Jamer et al. (2017)). The resistivity value varies from 107 $\mu\Omega cm$ to 98 $\mu\Omega cm$ from 2 K to 300K, respectively. The overall resistivity value is decreased compared to the parent. This was due to the substitution of Co in Mn_2FeAl, which enhances the charge carrier, and hence, a decrease in resistivity value is observed. The residual resistivity ratio $[RRR = \rho_{xx}(300K)/\rho_{xx}(2K)]$ for the present was found to be 0.915; the similar values are found for other Heusler systems also (Shahi et al. (2022)). The value of RRR indicates the presence of disorder in the system. Generally, in the case of a pure semiconductor, the resistivity follows an exponential behavior. Instead of this, here, the $\rho(T)$ data is modeled as the sum of both metallic and semiconducting contributions as given by the equations,

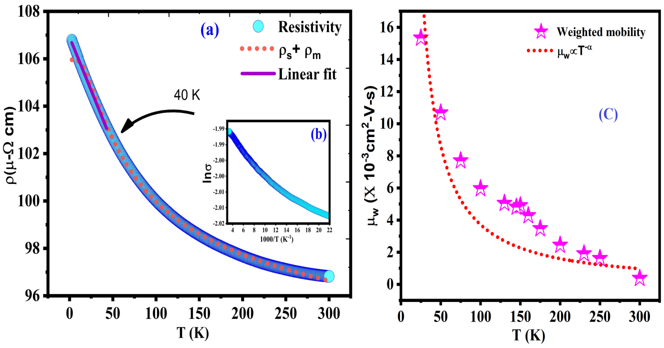

Fig. 4.3 (a)Temperature-dependent Resistivity of MCFA, fitted with equation 4.1 (orange dot line).(b) Inset shows the logarithmic scale of conductivity vs. 1000/T curve to determine the beginning of nonlinearity (c) Temperature variation of weighted mobility (μ_w) along with the temperature dependency of the order of $\alpha = 1.2$.

$$\rho_{xx}(T) = (\rho_0 + AT) + \rho_{(0)} exp\left(\frac{E_g}{2k_B T}\right) \tag{4.1}$$

Here, the first term with linear dependence provided the metallic contribution (ρ_m) and the exponential dependence provided the semiconductor contribution (ρ_s). ρ_0 is the residual resistivity (resistivity at 2 K), AT is a contribution term for electron-phonon scattering, and E_g is the band gap of the semiconductor. The above equation 4.1 is fitted well in the temperature region above a reference temperature of ($T_0 \sim 40K$).

The parameters obtained after the fitting is $\rho_0 \sim 106\ \mu\Omega cm$, $A = -0.0037\mu\Omega cmK^{-1}$ value, $E_g, \sim 9.81$ meV for the present system. The most peculiar result of the performed analysis is the negative sign of the coefficient A, which suggests that the phonon contribution to the transport behavior is negligible. So, this contribution is coming from the defects scattering rather than the phonons. The resistivity behavior for low temperatures (less than To) could be explained by a linear form of the resistivity

$$\rho_{xx} = \rho_0[1 + \gamma(T - T_0)] \tag{4.2}$$

Where γ is the temperature coefficient of resistivity, and T_0 is the reference temperature (mentioned above). After the linear fit of the equation, the obtained value of γ is $-8.4 \times 10^{-4} K^{-1}$. Along with the transport mechanism, it is also important to study the scattering between the charge carriers. To explain the scattering mechanism in the system, weighted mobility (μ_w), usually follows $T^{-\alpha}$ dependence, is calculated by the availability of S and ρ and can be calculated by the expression given in Ref (Snyder et al. (2020)). The variation of (μ_w) usually decreases with the temperature as shown in figure 4.3 (c). Generally, (μ_w) follows a $T^{-3/2}$ dependency for lightly doped semiconductors and suggests the presence of electron-phonon scattering in the system. For heavily doped semiconductors this dependency follows a $T^{-1/2}$ relation (Saurabh et al. (2022)). For MCFA, as shown in figure 4.3 (c) the value of α is 1.2, indicating alloy scattering. But the dependency slightly changes in the region around 100-150 K which is responsible for the occurrence of the peak in the S, discussed in the next section.

4.3.4 Thermopower and thermal conductivities

The S is measured in the temperature range of 25 K to 300 K, given in figure 4.4 (a). The S is found to be positive for the full temperature range. This is in accordance with the previous findings (Hinterleitner et al. (2020); Li et al. (2021); Seredina et al. (2019)) and indicates that the dominant carriers in MCFA are holes. The S at 300 K was found to be $3\mu V/K$, which then increased and attained a maximum value at 150 K, and after 150 K, it again started to decrease. A similar upturn behavior in S is also observed for other Heusler systems (Hinterleitner et al. (2020); Renard et al. (2014)).

This intriguing occurrence was observed in both the Seebeck and Raman spectra, i.e., at 150 K. In narrow gap semiconductors, it shows an extremum at a certain temperature. This maximum is due to the conduction of thermally excited electrons and holes across the

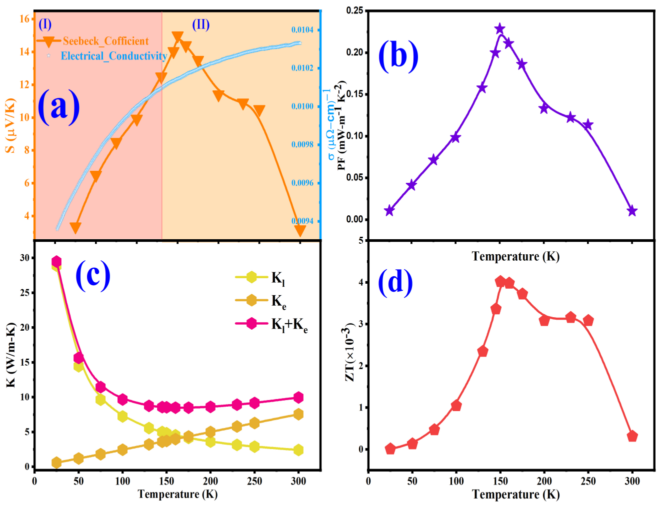

Fig. 4.4 Illustration of, (a) Seebeck coefficient and electrical conductivity of $Mn_{1.5}Co_{0.5}FeAl$ recorded from room temperature to 25 K. (b) Power factor (PF) for the system calculated using equation (5). (c) Thermal variations of thermal conductivity, electronic thermal conductivity (K_e) and lattice thermal conductivity (K_l). (d) Figure of merit (ZT) for the system. The lines are drawn as a guide to the eye.

pseudo gap Hinterleitner et al. (2020); Lue et al. (2007). The value of the band gap can be evaluated from the figure 4.4 (a), expression is given by),

$$E_g^* = 2e|S_{max}|T_{max}^S \tag{4.3}$$

after substituting the value of S_{max} and T_{max}^S the value of band gap is 2.2 meV. Despite the small initial value of the S at room temperature, we observed a significant increase to 15 $\mu V/K$ at 150 K, far exceeding the value of 2 $\mu V/K$ observed in Mn_2CoAl (Li et al. (2021)). The enhancement in S can be attributed to the presence of Fe, as Fe-based systems are widely recognized for their exceptional thermoelectric qualities (Garmroudi et al. (2022)) and high Seebeck constants at room temperature. Indeed, Fe has propelled to exhibit a relatively higher value than the Mn_2CoAl. In addition, the power factor (PF) is frequently used to measure the capacity of thermoelectric materials to convert a temperature gradient into electrical energy, which can be calculated by using the following relation,

$$PF = S^2\sigma \tag{4.4}$$

It attains a maximum of $2.2mW/mK^2$ at 150 K (figure 4.4) (a). Moreover, another important quantity used to evaluate the thermoelectric efficiency of a material is figure of merit (ZT). It depends on the σ and total thermal conductivity ($K_{tot} = K_e + K_l$), where K_e and K_l refers to the electronic and lattice thermal conductivity of the system. ($K_e = LT\sigma$), where L, is the Lorentz number 2.44×10^{-8} $W\Omega^{-2}$. On the other hand, K_l depends on the individual scattering mechanism, including grain boundaries, point defects, Umklapp processes, and electrons. K_l, when calculated under the Umklapp approach is given by

$$K_l = \Lambda \frac{M\theta_D^3\delta}{\gamma_G^2 n^{\frac{2}{3}} T} \tag{4.5}$$

where Λ is a constant (3.1×10^{-6}), M is the average atomic mass ($M = 48.67a.m.u$), δ^3 is the atomic volume (δ^3)= 63.48 (Å^3), n is the number of atoms in a primitive unit cell ($n = 4$), figure 4.3) (b) is used to determine the Debye temperature θ_D of the system which is in between the logarithmic scale of conductivity vs. 1000/T.

The temperature at which nonlinearity is started is the θ_D and for the present system it is 147 K. A comparable value of θ_D is also observed for the Mn_2FeAl system (Dash et al. (2020)). The Gruneisen parameter was calculated using the linear fit between $\ln\omega(T)$ and $\ln V(T)$ as shown in figure4.6 according to the following relation,

$$\gamma_G = -\frac{\partial ln\omega(T)}{\partial lnV(T)} \tag{4.6}$$

Where $V(T)$ is calculated from the temperature-dependent X-ray diffraction pattern along with the Lebeil, as shown in figure 4.5.

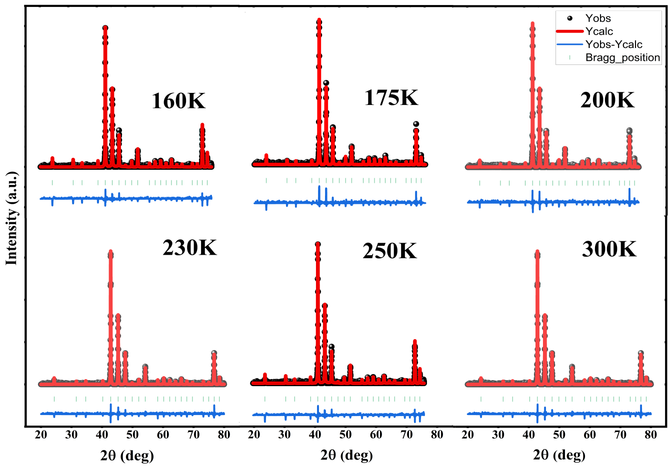

Fig. 4.5 Temperature dependent X-ray diffraction pattern of $Mn_{1.5}Co_{0.5}FeAl$.

The obtained values after refinement are summarised in table 4.1 1. The calculated value of γ_G is 1.86, for the present system, and it matches with the other systems also (Wang et al. (2022); Renard, Mori, Yamada, Tanaka, Miyazaki & Nishino (ade)). The estimated values of K_l and K_e are plotted in figure 4.4 (c) along with K_{tot}. It is observed that K_l tends to decrease as the temperature increases, which is consistent with the other findings (Ghosh et al. (2022)). However, K_e, which refers to the transfer of heat through the movement of free electrons within the materials, increases with increasing temperature. The reason behind this behavior can be attributed to the decrease in the resistivity of the system with increasing temperature figure 4.3 (a), which in turn increases the mobility of electrons. Therefore, a large number of electrons are available for the heat transfer. Additionally, in figure 4.4 (c), a peculiar phenomenon becomes apparent, characterized by a distinctive crossover between the K_l and the K_e. Above this temperature, the value of K_l surpasses the K_l. This phenomenon has also been observed in other Heusler alloys (Ding et al. (2015); Hayashi et al. (2020); Hori et al. (2020); Renard, Mori, Yamada, Tanaka, Miyazaki & Nishino (ade)). The observed crossover can be attributed to the behaviour of phonons in a normal semiconductor material.

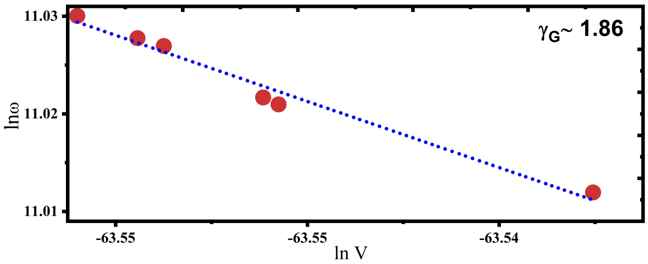

Fig. 4.6 Linear fit between lnV and $ln\omega$ for the estimation of γ_G

Traditionally, it is believed that once the temperature surpasses the θ_D, all phonons in the material start to vibrate. As the vibrations of phonons increase, the level of scattering also intensifies. Consequently, this leads to a decrease in the magnitude of K_l above θ_D. Further, the ZT is calculated after substituting the values obtained from the equations (4.5), (4.6), and K_{tot}. The ZT yields relatively low values of 0.2×10^{-3} at 300 K and higher value of 4×10^{-3} at 150 K. In traditional thermoelectric materials, S and σ are typically interdependent inversely to each other as a function of carrier concentration (Singh et al. (2018)). This will limit the improvement of the system's performance as if one is tried to increase one parameter the other will decrease due to inverse relation. Therefore, decoupling between the S and σ is the greatest challenge in thermoelectric systems. However, in the current study, we observed a decoupling between S and σ, indicated as region 1 in figure 4.3 (a). Here, in region 1 both S and σ. The decoupling for the present system is due to Co-doping, which enhances the charge carriers [47]. This decoupling allows us to independently control and optimize these properties, leading to a significant enhancement in ZT.

4.4 Conclusion

In summary, the thermoelectric properties of the system are examined, revealing that the S and PF initially increase monotonically up to 150 K. A significant increase in the S at 150 K, was due to the contribution of the thermally excited particles across their pseudo gap.

Table 4.1 Parameters obtained from temperature-dependent X-ray diffraction.

Temp.(K)	a(Å)	b(Å)	c(Å)	Volume(Å^3)
160	6.3062	6.3062	6.3062	250.7971
175	6.3100	6.3100	6.3100	251.2481
200	6.3102	6.3102	6.3102	251.2634
230	6.3141	6.3141	6.3141	251.7298
250	6.3142	6.3142	6.3142	251.7472
300	6.3323	6.3323	6.3323	253.9159

Likewise, the PF, ZT also attains a maximum value of $\sim 4 \times 10^{(-3)}$ at 150 K. Interestingly, a shift in the Raman spectra at the same temperature is observed. The calculated K_l and K_e showed a crossover behaviour at around 150 K. The crossover is attributed to the onset of lattice vibrations after the Debye temperature. Furthermore, the electronic properties of the Co-substituted Mn_2FeAl are also investigated. We confirmed that the observed electronic Raman spectra are solely attributed to crystal field splitting, and this is confirmed by XAS of transition metal elements. The electrical resistivity indicates the both semiconductor and metallic nature with a very narrow band gap of the order of 9 meV. Usually, semiconductor materials exhibit high Seebeck values, which motivated our research to identify potential candidates with promising thermoelectric properties for experimental realisation.